Author/s:
Balu, S;Greig, B;Wyithe, JSB

Title:
Fisher matrix forecasts on the astrophysics of galaxies during the epoch of reionization from the 21-cm power spectra

Date:
2023-10-01

Citation:
Balu, S., Greig, B. & Wyithe, J. S. B. (2023). Fisher matrix forecasts on the astrophysics of galaxies during the epoch of reionization from the 21-cm power spectra. Monthly Notices of the Royal Astronomical Society, 525 (2), pp.3032-3047. https://doi.org/10.1093/mnras/stad2552.

Persistent Link:
https://hdl.handle.net/11343/345364

Monthly Notices of the ROYAL ASTRONOMICAL SOCIETY

MNRAS **525,** 3032–3047 (2023) https://doi.org/10.1093/mnras/stad2552
Advance Access publication 2023 August 25

Fisher matrix forecasts on the astrophysics of galaxies during the epoch of reionization from the 21-cm power spectra

Sreedhar Balu [1,2]★ Bradley Greig [1,2] and J. Stuart B. Wyithe [1,2]

[1]*School of Physics, University of Melbourne, Parkville, VIC 3010, Australia*
[2]*ARC Centre of Excellence for All Sky Astrophysics in 3 Dimensions (ASTRO 3D) , Australia*

Accepted 2023 August 21. Received 2023 July 25; in original form 2023 May 8

ABSTRACT

The hyperfine 21-cm transition of neutral hydrogen from the early Universe ($z > 5$) is a sensitive probe of the formation and evolution of the first luminous sources. Using the Fisher matrix formalism we explore the complex and degenerate high-dimensional parameter space associated with the high-z sources of this era and forecast quantitative constraints from a future 21-cm power spectrum (21-cm PS) detection. This is achieved using MERAXES, a coupled semi-analytic galaxy formation model and reionization simulation, applied to an N-body halo merger tree with a statistically complete population of all atomically cooled galaxies out to $z \sim 20$. Our mock observation assumes a 21-cm detection spanning $z \in [5, 24]$ from a 1000 h mock observation with the forthcoming Square Kilometre Array, and is calibrated with respect to ultraviolet luminosity functions (UV LFs) at $z \in [5, 10]$, the optical depth of CMB photons to Thompson scattering from *Planck*, and various constraints on the IGM neutral fraction at $z > 5$. In this work, we focus on the X-ray luminosity, ionizing UV photon escape fraction, star formation, and supernova feedback of the first galaxies. We demonstrate that it is possible to recover five of the eight parameters describing these properties with better than 50 per cent precision using just the 21-cm PS. By combining with UV LFs, we are able to improve our forecast, with five of the eight parameters constrained to better than 10 per cent (and all below 50 per cent).

Key words: galaxies: evolution – galaxies: high redshift – dark ages, reionization, first stars.

1 INTRODUCTION

Following recombination, the early Universe entered the cosmic Dark Ages characterized by a neutral intergalactic medium (IGM) and the absence of luminous sources. The formation of the first stars and galaxies ushered in the era of the Cosmic Dawn. The intense ionizing ultraviolet (UV) radiation, characteristic of the young and massive stars, as well as X-rays (possibly from high-mass X-ray binaries, e.g. Mesinger, Ferrara & Spiegel 2013) impacted the thermal and ionization state of the IGM. This period was brought to its conclusion in the Epoch of Reionization (EoR) when the UV photons ionized the neutral hydrogen (H I) rendering it transparent to UV photons.

Considerable effort has been expended in the last few decades to unravel the complex physics of this period (see Mesinger 2019 and references therein). The forbidden 21-cm hyperfine transition signal is well-suited for this purpose because of its extreme sensitivity to the formation and evolution of the first stars and galaxies ($z \lesssim 30$), as well as the various feedback mechanisms in the early Universe. Though the ultimate goal of 21-cm interferometric experiments is to map the tomography of the IGM as a function of frequency (redshift), the first set of observations will be statistical in nature. The 21-cm signal is observed as a brightness temperature against a background source (which is almost always assumed to be the cosmic microwave background (CMB) radiation; e.g. Furlanetto, Peng Oh & Briggs 2006; Morales & Wyithe 2010; Pritchard & Loeb 2012). The 21-cm power spectrum (21-cm PS) quantifies the fluctuations in the brightness temperature of the 21-cm signal across the sky. Though a detection has yet to be made, current experiments such as the Murchison Widefield Array (MWA.[1]; Tingay et al. 2013), Low Frequency Array (LOFAR[2]; Van Haarlem et al. 2013), Hydrogen Epoch of Reionization Array (HERA[3]; Deboer et al. 2017) have already begun setting upper limits on the 21-cm PS (see Mertens et al. 2020; Trott et al. 2020; The HERA Collaboration 2022). The upcoming Square Kilometre Array (SKA[4]; Koopmans et al. 2014) will revolutionize 21-cm EoR cosmology with its unprecedented sensitivity.

The amplitude and shape of the 21-cm PS are extremely sensitive to the thermal and ionization state of the IGM (Barkana & Loeb 2001), and hence the astrophysics of early galaxy formation and evolution (Geil et al. 2016; Mesinger 2019). It is therefore imperative that realistic and efficient models (see Gnedin & Madau 2022 for a recent review) are available to interpret current and upcoming observations. Despite significant progress in this direction, there is considerable uncertainty about the properties of the underlying source populations of these models.

★ E-mail: bsreedhar@student.unimelb.edu.au

[1] www.mwatelescope.org
[2] www.astron.nl/telescopes/lofar
[3] reionization.org/
[4] www.skao.int

In this paper, we ask: *What can we learn about the underlying physical processes driving reionization from a successful detection of the 21-cm PS?* Simulating reionization requires large volumes ($\gtrsim 200\,h^{-1}$ Mpc according to Iliev et al. (2014); Kaur, Gillet & Mesinger (2020) for convergent reionization and 21-cm statistics). As a result, a number of models have been developed to make large-scale but computationally efficient realisations of the early Universe (e.g. Battaglia et al. 2013; Ghara, Choudhury & Datta 2015; Hassan et al. 2016; Choudhury & Paranjape 2018; Murray et al. 2020). To investigate the utility of the 21-cm PS as a probe of galaxy formation, MCMC methods have been utilized to place constraints on the parametrized properties (e.g. UV and X-ray) of population II & III star-forming galaxies (e.g. Greig & Mesinger 2015, 2017; Park et al. 2019; Qin et al. 2020, 2021a; Maity & Choudhury 2022; Bevins et al. 2023).

In this work, we use MERAXES (Mutch et al. 2016) – a semi-analytic model (SAM) of galaxy formation (see Somerville & Davé 2015 for a recent review) and evolution self-consistently coupled to a reionization model[5] – to forecast constraints on astrophysical properties of the early galaxies.

Unlike seminumerical models (for example, Mesinger, Furlanetto & Cen 2011; Choudhury & Paranjape 2018), which focus on population-averaged quantities (i.e. these models generally have no galaxies), MERAXES provides a realistic population of galaxies as sources of photons. MERAXES incorporates a detailed, physically motivated galaxy formation, and evolution model that includes baryonic infall, gas cooling, star formation, supernova feedback, AGN feedback, galaxy mergers, etc. Another essential feature of MERAXES, important for its application to reionization, is the simultaneous processing of all the galaxies in the simulation volume, thereby enabling the spatial coupling of reionization to galaxy evolution.

By efficiently coupling the reionization of the IGM via a modified version of 21CMFAST (Mesinger et al. 2011; Murray et al. 2020) and an underlying galaxy population sourced from a dark matter only *N*-body simulation, MERAXES is thus well-suited to explore the underlying parameter space of the complex astrophysics of this era. We deploy MERAXES on a $210\,h^{-1}$ Mpc cosmological simulation which resolves all the atomically cooled galaxies down from $z \sim 20$. The large-volume and high-mass resolution of our simulation make an MCMC analysis using MERAXES prohibitively expensive computationally.[6]

Using a Fisher matrix analysis, we forecast the constraints on a total of eight astrophysical parameters in our model that directly control the X-ray luminosity, UV escape fraction, star formation rates, and supernova feedback of the galaxies of the high-z Universe. Focusing on the upcoming SKA1-low, we forecast constraints from the 21-cm PS before exploring the improvements available when combining information from the UV LFs.

The paper is organized as follows: In Section 2, we introduce our *N*-body simulation (Section 2.1), galaxy SAM (Section 2.2), and the reionization model (Section 2.3). We also introduce our set of eight astrophysical parameters in this section. In Section 3, we introduce our mock observation, in Section 4, we describe the Fisher Matrix formalism and we analyse our results in Section 5. Our simulations use the best-fitting parameters from the Planck Collaboration (2016): $h = 0.6751, \Omega_m = 0.3121, \Omega_b = 0.0490, \Omega_\Lambda = 0.6879, \sigma_8 = 0.8150$, and $n_s = 0.9653$. All quantities quoted are in comoving units unless otherwise stated.

2 SIMULATING THE 21-CM SIGNAL

We give a brief review of our underlying dark matter-only *N*-body simulation and the MERAXES SAM in this section. We focus on a subset of the free parameters in our model that directly impact the star formation, supernova feedback, UV escape fraction, and X-ray luminosity of the galaxies.

2.1 N-body merger trees

We use the L210_N4320 dark matter-only *N*-body simulation of the *Genesis* suite of simulations (Power et al., in preparation). Containing 4320^3 particles in a 210^3 h^{-3} Mpc^3 volume, the simulation has a mass resolution of $\sim 5 \times 10^8$ h^{-1} $M_\odot$. L210_N4320 was run with the SWIFT (Schaller et al. 2018) cosmological code, using the VELOCIRAPTOR (Elahi et al. 2019a) halo identifier and merger trees generated using TREEFROG (Elahi et al. 2019b). The simulation consists of 120 snapshots between redshifts 30 and 5.

In order to resolve haloes down to the atomic cooling limit at $z = 20$, the L210_N4320 simulation was augmented using the Monte Carlo algorithm-based code DARKFOREST (Qiu et al. 2020) achieving an effective halo mass resolution of $\sim 2 \times 10^7$ h^{-1} $M_\odot$ (L210_AUG of Balu et al. 2023). DARKFOREST achieves this by sampling from a conditional mass function based on the extended Press–Schechter theory (Bond et al. 1991; Bower 1991; Lacey & Cole 1993) that has been modified to match the halo mass functions from *N*-body simulations. These new low-mass haloes are introduced into the simulation volume and appended to the merger trees. Importantly, DARKFOREST also assigns positions to these newly added haloes based on the local halo density field (Ahn et al. 2015) and the linear halo bias (Tinker et al. 2010). For the rest of this work, we use L210_AUG as our fiducial simulation.

2.2 A realistic galaxy population from MERAXES

MERAXES (Mutch et al. 2016) contains detailed and physically motivated prescriptions for galaxy formation and evolution. These include, for example, gas infall into dark matter haloes from the IGM followed by its radiative cooling and subsequent star formation, as well as eventual supernova feedback and metal enrichment of the interstellar medium (ISM). Active galactic Nuclei (AGN) feedback from central black holes of the galaxies was implemented in Qin et al. (2017) and calculations of the galaxies' UV luminosity in Qiu et al. (2019). In addition, MERAXES also has a coupled treatment of reionization based on the 21CMFAST seminumerical code (Mesinger et al. 2011; Murray et al. 2020, see Section 2.3 for more details). In the following sections, we give detailed but non-exhaustive descriptions of the various physics implementations pertinent to our astrophysical model. Table 1 lists the free parameters of our model along with their adopted fiducial values.

2.2.1 *Star formation prescription*

At every snapshot, the baryonic content of a dark matter halo increases by $(1 - f_{mod}) f_b M_{vir}$, where $f_b = \Omega_b/\Omega_m$ is the baryonic

[5]For alternate approaches see (e.g. Seiler et al. 2019; Visbal, Bryan & Haiman 2020; Hutter et al. 2021; Ma et al. 2023)

[6]Recently, Mutch et al. (2023) utilized MERAXES to place constraints on the UV escape fraction of the early galaxies using existing high-z observations within an MCMC framework. This was only feasible owing to (i) not considering the thermal state of the IGM and (ii) using a simulation volume 30 times smaller with a 6 times lower mass resolution for the galaxies.

Table 1. The first column lists the free astrophysical model parameters for which we forecast the uncertainties with a Fisher matrix formalism. The next three columns give a short description, the corresponding equation in the text, and their adopted fiducial values in this work respectively. The fifth and sixth columns list the forecasted 1σ constraints using just the 21-cm PS and just the UV LFs, respectively, and the final column gives the same for a joint analysis of both the 21-cm and the UV LFs. The fractional uncertainties are given in brackets as a percentage. We do not vary the X-ray parameters, L_X/SFR, and E_0, for the UV LFs analysis as they do not have an impact on the UV LFs.

Parameter	Description	Equation	Fiducial value	21-cm PS alone 1σ values (% uncertainty)	UV LF alone 1σ values (% uncertainty)	21-cm PS & UV LF 1σ values
$\log_{10}\left(\frac{L_X}{\mathrm{SFR}}\right)$	X-ray luminosity per SFR	(14)	40.50	0.0043 (1.1×10^{-2})	–	0.0027 (7.0×10^{-3})
E_0	Minimum X-ray photon energy	(14)	500.00	54.5058 (10.9)	–	27.708 (5.54)
$f_{\mathrm{esc},0}$	Escape fraction normalization	(10)	0.14	0.0092 (6.55)	0.1172 (83.71)	0.0069 (4.91)
α_{esc}	Escape fraction redshift scaling	(10)	0.20	0.1339 (66.93)	0.2552 (127.6)	0.0965 (48.25)
$\log_{10}(\Sigma_{\mathrm{SF}})$	Critical mass normalization	(1)	− 1.86	4.3496 (233.9)	0.9511 (51.13)	0.7401 (39.8)
$\log_{10}(\alpha_{\mathrm{SF}})$	Star formation efficiency	(2)	− 1.00	0.0883 (8.82)	0.0661 (6.61)	0.0436 (4.35)
$\log_{10}(\epsilon_0)$	Supernova ejection efficiency	(8)	0.19	0.0470 (25.1)	0.0668 (35.16)	0.0309 (16.56)
$\log_{10}(\eta_0)$	Supernova reheat efficiency	(9)	0.84	0.9876 (117.03)	0.0991 (11.8)	0.0658 (7.803)

fraction and f_{mod} (equation 16) is the baryon fraction modifier – set by the local IGM ionization state from the previous snapshot – coupling galaxy growth to the ionization state of the IGM (see Section 2.3.2 for details), and M_{vir} is the halo virial mass. This newly accreted baryonic gas is deposited to a 'hot-gas reservoir' of the halo from where it cools radiatively to a 'cold-gas component' from which it can form stars.

Star formation in MERAXES follows the disc stability argument of Kauffmann (1996), wherein gas participates in star formation when the cold-gas mass is higher than a critical mass (m_{crit}) given by

$$m_{\mathrm{crit}} = \Sigma_{\mathrm{SF}}\left(\frac{V_{\mathrm{max}}}{100\mathrm{kms}^{-1}}\right)\left(\frac{r_{\mathrm{disc}}}{10\mathrm{kpc}}\right) \times 10^{10}\mathrm{M}_{\odot}, \tag{1}$$

where Σ_{SF} is the critical mass normalization, V_{max} is the maximum halo circular speed, and r_{disc} is the scale radius of the galactic disc. The new stellar mass, ΔM_{star}, formed in the time-step Δt is given by

$$\Delta M_{\mathrm{star}} = \alpha_{\mathrm{SF}}\frac{m_{\mathrm{cold}} - m_{\mathrm{crit}}}{t_{\mathrm{dyn,disc}}}\Delta t, \tag{2}$$

where α_{SF} is the star formation efficiency, m_{cold} is the mass locked up in the cold-gas component, and $t_{\mathrm{dyn,disc}}$ is the dynamical time of the disc given by $r_{\mathrm{disc}}/V_{\mathrm{max}}$.

In this work, both Σ_{SF} and α_{SF} are free parameters in our astrophysical model whose fractional uncertainty we predict in Section 5.

2.2.2 *Supernova feedback prescription*

The star formation rates and the stellar mass of galaxies are regulated by a number of feedback mechanisms including supernovae (SNe) feedback from evolved stars, AGN feedback, and the ionization state of the IGM regulated by the progress of reionization. Mutch et al. (2016) showed that SNe feedback dominates over self-regulation by the EoR. In this subsection, we detail the SNe implementation in our model.

The primary impact of SNe feedback is to heat the gas reservoirs of the halo resulting in the transfer of the gas from the cold to the hot gas reservoirs and in extreme cases the removal of the gas from the hot halo (i.e. altogether from the galaxy). Our implementation, modified from Guo et al. (2011) to take advantage of our high-cadence merger trees (see Qiu et al. 2019), is based on energy conservation. The total stellar mass going SNe (Δm_{new}) at a particular snapshot of the simulation depends on both the current and previous star formation.[7] To account for this, we track the stars formed in the present and four previous snapshots. The stellar mass going SNe at a particular snapshot is calculated as a weighted average star formation history

$$\Delta m_{\mathrm{new}} = \frac{\int_t^{t+\Delta t} \mathrm{d}t' \int_0^{\infty} \mathrm{d}\tau \frac{\mathrm{d}\varepsilon}{\mathrm{d}\tau}\psi\left(t'-\tau\right)}{\int_0^{\infty} \mathrm{d}\tau \frac{d\varepsilon}{\mathrm{d}\tau}}, \tag{3}$$

where Δt is the simulation time-step, $\mathrm{d}\varepsilon/\mathrm{d}\tau$ is the rate of energy release per unit stellar mass via Type-II SN by stars within age τ and $\tau + \mathrm{d}\tau$, and $\psi(t)$ is the star formation rate at time t of the galaxy. We calculate $\mathrm{d}\varepsilon/\mathrm{d}\tau$ from STARBURST99 (Leitherer et al. 1999, 2010, 2014) accounting for both metallicity as well as a Kroupa (2002) initial mass function. The energy released by SNe can then be calculated as

$$\Delta E_{\mathrm{SN}} = \epsilon \int_t^{t+\Delta t} \mathrm{d}t' \int_0^{\infty} \mathrm{d}\tau \frac{\mathrm{d}\varepsilon}{\mathrm{d}\tau}\psi\left(t'-\tau\right), \tag{4}$$

where ϵ is the energy coupling efficiency.

The amount of gas reheated from the cold gas reservoir ($\Delta m_{\mathrm{reheat}}$) or ejected altogether from the halo ($\Delta m_{\mathrm{eject}}$) is calculated as

$$\Delta m_{\mathrm{reheat}} = \begin{cases} \eta\Delta m_{\mathrm{new}}, & \Delta E_{\mathrm{SN}} \geq \Delta E_{\mathrm{hot}} \\ \dfrac{\Delta E_{\mathrm{SN}}}{1/2V_{\mathrm{vir}}^2}, & \Delta E_{\mathrm{SN}} < \Delta E_{\mathrm{hot}} \end{cases}, \tag{5}$$

[7] As the largest time-step of our simulation is ∼16 Myr, newly formed massive stars can go SNe in the same time-step and less-massive stars can survive for a few snapshots.

and

$$\Delta m_{\rm eject} = \frac{\Delta E_{\rm SN} - \Delta E_{\rm hot}}{1/2 V_{\rm vir}^2}, \tag{6}$$

where

$$\Delta E_{\rm hot} = \frac{1}{2}\eta \Delta m_{\rm new} V_{\rm vir}^2, \tag{7}$$

η is the mass loading factor and $V_{\rm vir}$ is the halo virial velocity. Following Qiu et al. (2019), ϵ and η are implemented as

$$\epsilon = \begin{cases} \epsilon_0 \left(\frac{1+z}{4}\right) \left(\frac{V_{\rm max}}{70\ {\rm kms}^{-1}}\right)^{-1}, & V_{\rm max} \geq 70\ {\rm kms}^{-1} \\ \epsilon_0 \left(\frac{1+z}{4}\right) \left(\frac{V_{\rm max}}{70\ {\rm kms}^{-1}}\right)^{-3.2}, & V_{\rm max} < 70\ {\rm kms}^{-1}, \end{cases} \tag{8}$$

and,

$$\eta = \begin{cases} \eta_0 \left(\frac{1+z}{4}\right)^2 \left(\frac{V_{\rm max}}{60{\rm kms}^{-1}}\right)^{-1}, & V_{\rm max} \geq 60\ {\rm kms}^{-1} \\ \eta_0 \left(\frac{1+z}{4}\right)^2 \left(\frac{V_{\rm max}}{60\ {\rm kms}^{-1}}\right)^{-3.2}, & V_{\rm max} < 60\ {\rm kms}^{-1}, \end{cases} \tag{9}$$

respectively, where $V_{\rm max}$ is the maximum halo circular velocity, ϵ_0 is the supernova energy coupling normalization, and η_0 is the supernova ejection efficiency.

We forecast the fractional uncertainty on both ϵ_0 and η_0 and summarize their values in Table 1.

2.2.3 *Escape fraction of the UV ionizing photons*

The fraction of ionizing photons escaping into the IGM from galaxies plays an important role in regulating the ionization fraction and morphology. The model parameters that directly impact the ionization state have a pronounced effect on the 21-cm PS. Following Mutch et al. (2016) we employ an escape fraction ($f_{\rm esc}$) prescription for galaxies that is solely redshift dependent (though see e.g. Kimm et al. 2017; Yeh et al. 2023). This results in an $f_{\rm esc}$ that is skewed towards higher z, motivated by two factors. First, it is easier for the photons to climb out of the shallower potential well of low-mass high-z galaxies. Secondly, early galaxies are also characterized by less dust attenuation compared to their low-redshift counterparts

$$f_{\rm esc} = f_{\rm esc,0} \left(\frac{1+z}{6}\right)^{\alpha_{\rm esc}}. \tag{10}$$

We allow both the escape fraction normalization $f_{\rm esc,0}$ and redshift scaling $\alpha_{\rm esc}$ to be free parameters in this work.

2.3 Evolution of the IGM

The thermal evolution and ionization state of the IGM follows 21CMFAST (Mesinger et al. 2011; Murray et al. 2020), modified to take advantage of our realistic galaxy population. MERAXES sources the dark matter density and velocity fields from the underlying N-body simulation. We begin by gridding our simulation volume and assigning the galaxies to voxels based on their positions. In the present work, motivated by the typical $H\,ii$ bubble sizes during the EoR (Furlanetto, Zaldarriaga & Hernquist 2004, Wyithe & Loeb 2004), we divide our simulation into 1024^3 voxels corresponding to a cell dimension of $\sim$0.21 h^{-1} Mpc. We give a brief summary of our method in the following subsections.

2.3.1 *Thermal state of the IGM*

The thermal state of a H I cloud, characterized by the spin temperature $T_{\rm S}$, depends upon the radiation that is impinging upon it. Even though $T_{\rm S}$ is influenced by both UV and X-ray photons, the latter has a considerably more pronounced impact (e.g. Mesinger et al. 2013) and is computed as

$$T_{\rm S}^{-1} = \frac{T_{\rm CMB}^{-1} + x_\alpha T_\alpha^{-1} + x_{\rm c} T_{\rm K}^{-1}}{1 + x_\alpha + x_{\rm c}}, \tag{11}$$

where $T_{\rm CMB}$ is the temperature of the CMB, $T_{\rm K}$ is the gas kinetic temperature, T_α, which we take to be equal to $T_{\rm K}$, is the colour temperature, x_α is the Wouthuysen–Field coupling constant (Wouthuysen 1952; Field 1958), and $x_{\rm c}$ is the collisional coupling coefficient which accounts for the collisional coupling of the gas with other H I atoms, free electrons, and free protons. Here, we summarize only the implementation of the X-rays (which largely impacts the $T_{\rm K}$) and refer the reader to Balu et al. (2023) for further details.

An X-ray photon with energy E_e when emitted at redshift $z^{'}$, redshifts to energy $E = E_e(1+z)/(1+z^{'})$ at redshift z. We compute the comoving X-ray emissivity $\epsilon_X(\boldsymbol{x}, E_e, z')$ in the emitted frame at location $\boldsymbol{x}$ as

$$\epsilon_X(\boldsymbol{x}, E_e, z') = (L_{\rm X}^{'}/{\rm SFR}) \times {\rm SFRD}(\boldsymbol{x}, z'), \tag{12}$$

where $L_{\rm X}^{'}/{\rm SFR}$ is the specific X-ray luminosity per SFR[8] and ${\rm SFRD}(\boldsymbol{x}, z')$ is the star formation rate density. The *SFRD* grid depends on the local galaxy population, enabling us to couple galaxy evolution with the thermal state of the IGM. $L_{\rm X}^{'}/{\rm SFR}$ is implemented as a power-law of the X-ray energy as

$$L_{\rm X}^{'}/{\rm SFR} \propto E^{-\alpha_X}, \tag{13}$$

where α_X is the X-ray spectral index and is normalized as

$$L_{\rm X}/{\rm SFR} = \int_{E_0}^{2{\rm keV}} {\rm d}E_e L_{\rm X}^{'}/{\rm SFR}. \tag{14}$$

$L_{\rm X}/{\rm SFR}$ is one of the free parameters of our model and has units [erg s^{-1}M$_\odot^{-1}$yr].[9] We impose an upper limit of 2 keV since X-ray photons with higher energies have mean-free paths longer than the Hubble length and are unlikely to impact $T_{\rm S}$ (McQuinn 2012; Das et al. 2017). The lower limit E_0 is motivated by the absorption of low-energy X-rays within the galaxy itself.

We forecast constraints on both E_0 and $L_{\rm X}/{\rm SFR}$ in this work, and their fiducial values are summarized in Table 1.

2.3.2 *Ionization state of the IGM*

We compute the ionization ($x_{H\,ii}$) grid by employing an excursion-set formalism (Furlanetto et al. 2004) by comparing the total number of ionizing photons to the combined number of neutral atoms and recombinations within spheres of decreasing radii. Grid voxels inside a sphere of radius R, with centre $\boldsymbol{x}$, and at redshift z are deemed to be ionized if

$$N_{\rm b*}(\boldsymbol{x}, z|R) N_\gamma f_{\rm esc} \geq N_{\rm atom}(\boldsymbol{x}, z|R)(1 + \bar{n}_{\rm rec})(1 - \bar{x}_e), \tag{15}$$

where $N_{\rm b*}(\boldsymbol{x}, z|R)$ is the cumulative number of stellar baryons, N_γ is the average number of ionizing photons per stellar baryon, and $f_{\rm esc}$ is their escape fraction. The left-hand side of equation (15) thus gives

[8]Note that this SFR is an average quantity of all the galaxies in a grid and is different from the ψ in equation (3), which is for each galaxy.
[9]Note, our $L_{\rm X}/{\rm SFR}$ is equivalent to $L_{\rm X<2keV}/{\rm SFR}$ in 21CMFAST.

the total number of ionizing photons in the volume. On the right-hand side, $N_{\rm atom}(\boldsymbol{x}, z|R)$ is the total number of baryons, $(1+\bar{n}_{\rm rec})$ accounts for the recombinations inside Lyman limit systems (see Sobacchi & Mesinger 2014), and $(1-\bar{x}_e)$ accounts for secondary ionizations caused by the X-ray photons, giving the number of neutral H I atoms in the same volume. We fix the maximum value of R to be 50 Mpc (see Songaila & Cowie 2010; Becker et al. 2021).

The number of stellar baryons, $N_{\rm b*}$, is inferred from the stellar mass that is dependent on the star formation histories of all star-forming galaxies. We compute a $f_{\rm mod}$ for each galaxy based on their local $x_{\rm H\,I}$ value, enabling us to couple a galaxy's growth to its local IGM ionization state. In the next snapshot, the amount of fresh gas accreting on to the galaxy is modulated by $f_{\rm mod}$ which is calculated, following Sobacchi & Mesinger (2013), as

$$f_{\rm mod} = 2^{-M_{\rm filt}/M_{\rm vir}}, \tag{16}$$

where $M_{\rm filt}$ is the 'filtering mass', corresponding to when the baryon fraction of the host halo is half of the cosmic IGM value and is given by

$$M_{\rm filt} = M_0 J_{21}^a \left(\frac{1+z}{10}\right)^b \left[1-\left(\frac{1+z}{1+z_{\rm ion}}\right)^c\right]^d, \tag{17}$$

where z is the current redshift, $z_{\rm ion}$ is the redshift when the voxel was first ionized, and J_{21} is the local average UVB. The values [M_0, a, b, c, d] are taken from (Sobacchi & Mesinger 2013) (see Mutch et al. 2016 for more details). In this manner, by coupling galaxy growth to the local ionization state as well as the local UV ionizing background, MERAXES enables a self-consistent reionization scenario. See Geil et al. (2016) for an exploration of the self-consistent and UV background regulated reionization within MERAXES .

2.4 21-cm brightness temperature

A radio telescope measures the brightness temperature ($\delta T_{\rm b}$) of a H I cloud, which is the offset of the spin temperature ($T_{\rm S}$) against a background radiation source (assumed to be the CMB) of temperature T_γ as a function of frequency ν, given by

$$\begin{aligned}\delta T_{\rm b}(\nu) &= \frac{T_{\rm S}-T_\gamma}{1+z}(1-e^{-\tau_{\nu_0}}) \\ &\approx 27 x_{\rm H\,I}(1+\delta_{\rm nl})\left(\frac{H}{{\rm d}v_r/{\rm d}r+H}\right)\left(1-\frac{T_\gamma}{T_{\rm S}}\right) \\ &\quad\times\left(\frac{1+z}{10}\frac{0.15}{\Omega_{\rm M}h^2}\right)\left(\frac{\Omega_{\rm b}h^2}{0.023}\right){\rm mK},\end{aligned} \tag{18}$$

where τ_{ν_0} is the optical depth at the 21-cm transition frequency ν_0, $x_{\rm H\,I}$ is the neutral hydrogen fraction, $\delta_{\rm nl}$ is the fluctuations in the underlying dark matter density field, H is the Hubble parameter, and ${\rm d}v_r/{\rm d}r$ is the line-of-sight component of the radial derivative of the peculiar velocity. All of the terms in equation (18) are evaluated at $z = \nu_0/\nu - 1$.

3 FIDUCIAL SIMULATION AND MOCK OBSERVATIONS

In this section, we describe our fiducial model as well as the mock observations which are used to forecast constraints on our astrophysical model parameters.

3.1 Fiducial model parameters

The L210_AUG simulation from Balu et al. (2023) was calibrated against existing observables including UV LFs from Bouwens et al. (2015,2021), and stellar mass functions from Song et al. (2016) and Stefanon et al. (2021). The reionization history was calibrated using the Thomson scattering optical depth of free electrons to CMB photons from the Planck Collaboration (2020) (see figs 3 and 4 of Balu et al. 2023).

The fiducial values of our eight astrophysical model parameters are given in the fourth column of Table 1. These parameters can be divided into four groups of two in the order they are shown in the table, having direct control on the X-ray properties ($L_{\rm X}$/SFR and E_0), the ionizing UV photon escape fraction ($f_{\rm esc,0}$ and $\alpha_{\rm esc}$), star formation ($\Sigma_{\rm SF}$ and $\alpha_{\rm SF}$), and the supernova feedback (ε_0 and η_0) of the galaxies.

3.2 21-cm power spectra

The frequency dependence of the 21-cm signal imparts a line-of-sight evolution to the 21-signal. To account for this, MERAXES produces a 21-cm light-cone by stitching together (linearly) interpolated $\delta T_{\rm b}$ co-evolution grids. Following Greig & Mesinger (2018), we subdivide our 21-cm light-cone into cubical grids of a size equivalent to our simulation volume (1024^3) and calculate the spherically averaged dimensionless 21-cm PS in each (shown as the solid blue curve in Fig. 1). We obtain 11 redshift chunks spanning $z \in [5, 24]$, and assign redshift values to them corresponding to the mid-point of each chunk.

3.3 Modelling observational noise

The sensitivity of a radio interferometer to the 21-cm PS can be divided into two components: (1) thermal noise, which is important on the small scales and (2) sample (cosmic) variance, prominent on the large scales. The total noise power $\sigma[\Delta^2_{21}(k)]$ is given by adding these two in quadrature:

$$\left[\frac{1}{\sigma[\Delta^2_{21}(k)]}\right]^2 = \sum_i \left(\frac{1}{\Delta^2_{{\rm N},i}+\Delta^2_{21}}\right)^2, \tag{19}$$

where $\Delta^2_{\rm N}(k)$ is the thermal noise given by (Morales 2005; McQuinn et al. 2006; Parsons et al. 2012):

$$\Delta^2_{\rm N}(k) \approx X^2 Y \frac{k^3}{2\pi^2}\frac{\Omega'}{2t}T^2_{\rm sys}, \tag{20}$$

where X and Y relate the bandwidths and solid angles to the comoving distance to the source, Ω' is a factor dependant on the beam of the telescope (see Parsons et al. 2014), t is the integration time for the mode k, and $T_{\rm sys}$ is the system temperature given by $T_{\rm sys} = T_{\rm sky} + T_{\rm rec}$ with $T_{\rm sky}$ and $T_{\rm rec}$ being the sky and receiver temperature, respectively. The quadrature addition and the form of the cosmic variance noise in equation (19) assume that the errors are Gaussian distributed, which is reasonable for the relevant scales in this work (see Qin et al. 2021a, b; Prelogović & Mesinger 2023).

In this work, we focus on a future observation of the 21-cm PS by the SKA. We limit our attention to the upcoming first phase of SKA – the so-called SKA1-low.[10] We only include the stations in the 'Central Area' of the SKA1-low, resulting in 296 stations of diameter 35 m distributed across a circular area with 1.7 km diameter, we calculate the interferometer's sensitivity to the 21-cm PS using the 21CMSENSE .[11] PYTHON package (Pober et al. 2013, 2014). We assume an observational campaign corresponding to six hours per night for 180 d, i.e. a total of 1080 h, and sky

[10] See the official SKA1 System Baseline Design document for further details.
[11] www.github.com/steven-murray/21cmSense

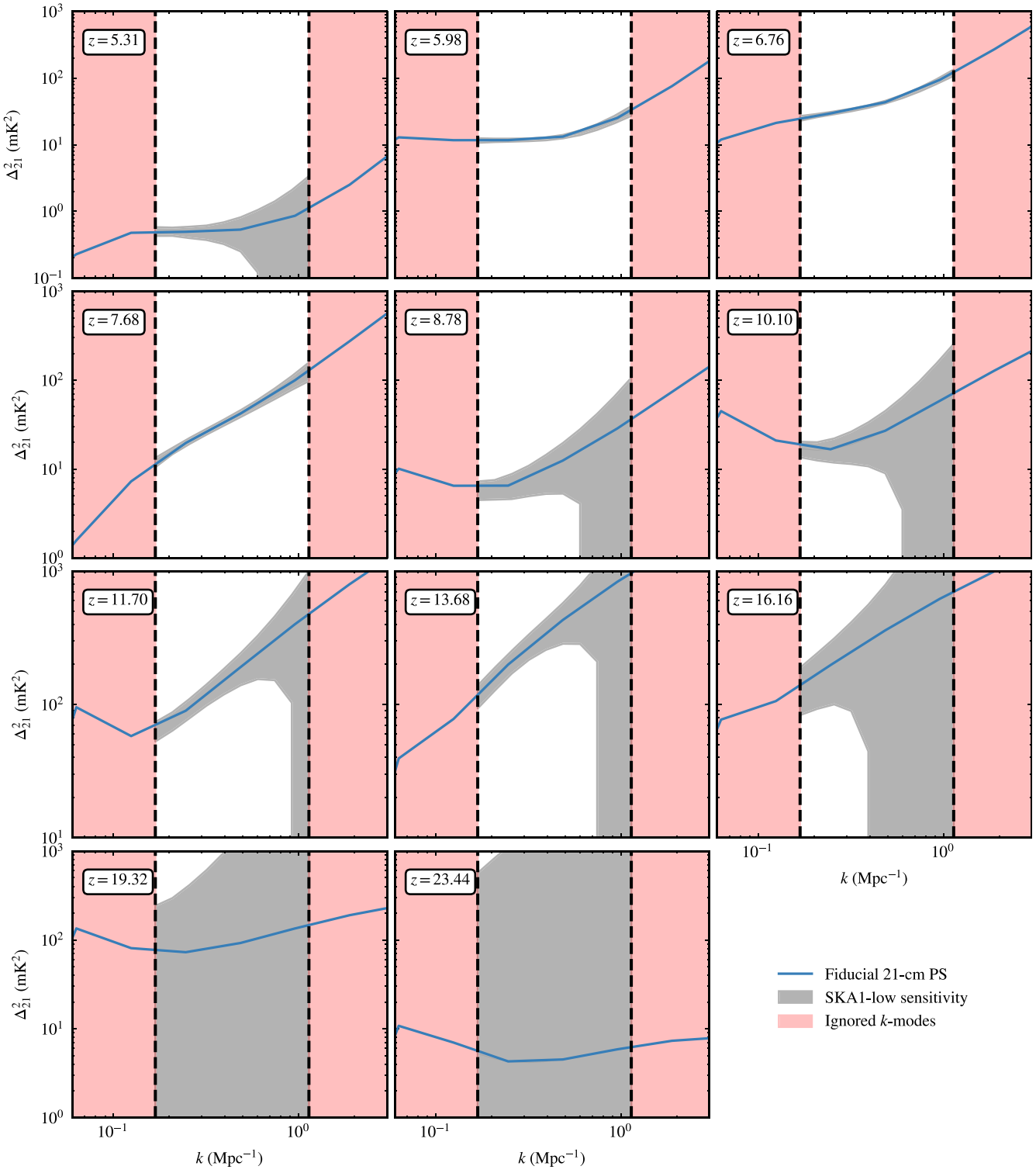

Figure 1. The blue curve shows the dimensionless 21-cm PS Δ^2_{21} (mK^2) from our fiducial model. The grey-shaded region represents the sensitivity (including both thermal and cosmic variance noise) to the 21-cm PS for a 1000 h observation with the upcoming SKA1-low. We use the 'moderate' foreground removal case from Pober et al. 2014, effectively ignoring (pink-shaded region) all the k-modes falling within the 21-cm foreground wedge (setting a $k_{\rm min} = 0.16$ Mpc^{-1}). The $k_{\rm max} = 1.4$ Mpc^{-1} is set by a combination of the spatial scales resolved by SKA1-low (set by the longest baseline in our model for the core) as well as scales we trust not to be dominated by the Poisson noise of the sources.

temperature $T_{\rm sky}$ to be dominated by galactic synchrotron emission (Thompson, Moran & Swenson 2017) scaling with frequency ν as $T_{\rm sky} = 60(\nu/300{\rm MHz})^{-2.55}{\rm K}$. Additionally, assuming that the telescope reflects 10 per cent of the response to the sky (Pober et al. 2014), we set $T_{\rm rec} = 40{\rm mK} + 0.1{\rm T_{sky}}$. We combine partially coherent baselines to improve power-spectrum sensitivity and use the 'moderate' foreground removal scenario of 21CMSENSE, wherein we avoid the modes that are contained within the so-called foreground wedge (Datta, Bowman & Carilli 2010) extending $k_{\parallel} = 0.1\,{\rm h\ Mpc^{-1}}$ beyond the horizon limit. As we ignore the modes that fall within the foreground wedge, we are limited to $k_{\rm min} = 0.16\ {\rm Mpc^{-1}}$ for our analysis. We also have an upper limit of $k_{\rm max} = 1.4\ {\rm Mpc^{-1}}$ which arises from a combination of both the spatial scales that are probed by the SKA1-low (set by the longest baseline we consider in our modelling of the array), as well as Poisson, shot noise from our simulation. Fig. 1 shows the PS noise (grey shaded region) that is generated for our fiducial 21-cm PS. The red-shaded region shows k-modes that are ignored in this work.

3.4 Luminosity Functions

In addition to exploring the possible constraints on our fiducial model from the 21-cm PS, we also consider the improvements that are achievable with a joint analysis of both the 21-cm PS and the UV LFs.

In addition to updates on the SNe feedback (see Section 2.2.2), Qiu et al. (2019) explored different implementations of dust attenuation in MERAXES . Here, we adopt the parametrization for the UV optical depth that depends on the dust-to-gas ratio (Charlot & Fall 2000) of the galaxies. The model differentiates between a short-lived birth cloud of the stars as well as the ISM of the galaxy. Photons are absorbed by both the birth cloud (albeit for a short while until it gets depleted by star formation) and the ISM. The free parameters of MERAXES – particularly the ones impacting the galaxy physics – have been calibrated (see Qiu et al. 2019; Balu et al. 2023) to their fiducial values against infrared excess (IRX)-β, UV LFs, and stellar mass functions at $z > 5$.

The blue curves in Fig. 2 are the UV LFs from our calibrated simulation. The error bars are determined by multiplying our simulated UV LF data by the corresponding fractional uncertainty on each data point from the Bouwens et al. (2021) observational data. In addition to the 21-cm PS, we thus have six UV LFs from $z \in [5, 10]$.

4 FORECASTS USING FISHER MATRICES

To place quantitative constraints on the model parameters we use the Fisher information matrix ($\mathbf{F}_{ij}$; Tegmark, Taylor & Heavens 1997; Albrecht et al. 2009). For any set of observations, the Fisher matrix provides the best possible constraints on the parameters of an assumed model. An implicit assumption is that the errors on these parameters are Gaussian and that the observational data points are statistically independent. In this limit, by the Cramer–Rao theorem, the covariance matrix ($\mathbf{C}_{ij}$) of the parameters is given by the inverse of the Fisher matrix

$$\mathbf{C}_{ij} = \mathbf{F}_{ij}^{-1}. \tag{21}$$

The 1σ error on the ith parameter is given by the corresponding term on the diagonal of the covariance matrix i.e. $\mathbf{C}_{ii}$. Another relevant property of the Fisher matrices is their additive nature enabling one to do joint analyses of a different set of observations. This is achieved by adding the corresponding Fisher matrices together before calculating the joint $\mathbf{C}_{ij}$.

Given the likelihood function L (the probability of the data given the model parameters θ) $\mathbf{F}_{ij}$ is given by

$$\mathbf{F}_{ij} \equiv -\left\langle \frac{\partial^2 \ln L}{\partial\theta_i \partial\theta_j} \right\rangle. \tag{22}$$

For the present work, we compute $\mathbf{F}_{ij}$ as

$$\mathbf{F}_{ij} = \sum_{k,z} \frac{1}{\sigma^2(k,z)} \frac{\partial\Delta^2(k,z)}{\partial\theta_i} \frac{\partial\Delta^2(k,z)}{\partial\theta_j}, \tag{23}$$

where $\Delta^2(k, z)$ is the dimensionless 21-cm PS, $\sigma(k, z)$ is the observational uncertainty on a measured $\Delta^2(k, z)$ (see equation 19), and the summation is over all the k-modes and z-bins. Fisher matrices are thus sensitive to the derivatives of the 21-cm PS, with a larger value indicating increased sensitivity of the statistic to the model parameter. This translates into tighter constraining power on the model parameter. Parameters with a similar structure for the derivatives, as a function of k, will be degenerate (Pober et al. 2014). In Fig. A1 of appendix A, we show the noise $[\sigma(k, z)]$ weighted derivatives of the 21-cm PS with respect to each parameter we study in this work. Fig. 1 makes it evident that the noise levels corresponding to a $\sim$1000 h observation with SKA1-low is lowest for the redshifts $z \lesssim 8$. Thus, from equation (23), the constraining power will be dominated by these redshifts. Since the 21-cm PS is sensitive to different astrophysical parameters at different epochs (Furlanetto et al. 2006), this will be reflected in our forecasted constraints.

Except for E_0, $f_{\rm esc,0}$ and $\alpha_{\rm esc}$, all other parameters are varied in log-space as they can vary by at least an order of magnitude. For calculating the Fisher matrix we vary each parameter by ±4 per cent around its fiducial value.[12] In order to further avoid numerical artefacts while computing the derivatives, we fitted the mock 21-cm PS with a 5$^{\rm th}$-order polynomial in log-space and interpolated the values for k-bins evenly spaced in $\log_{10}(k)$.[13]

The $\mathbf{F}_{ij}$ corresponding to the UV LFs are computed by appropriately modifying equation (23). Fig. B1 shows the derivatives of the UV LFs with respect to our model parameters after being weighted by the error $[\sigma(M_{\rm UV}, z)]$. We note here that while constructing the Fisher matrix corresponding to the UV LFs, we do not consider the ones varying the X-ray properties (i.e. E_0 and $\log_{10}({\rm L_X/SFR})$) as they do not have any impact on the galaxy properties which affect its luminosity.[14]

The primary advantage of a Fisher matrix analysis is the associated computational efficiency as they are quick and easy to calculate. This is particularly important when a single model evaluation is too computationally expensive for an MCMC, as is the case for MERAXES .[15]

[12] We explored different choices of the step-size and (visually) ensured the convergence of the derivatives.

[13] Polynomial fitting with different orders as well as in linear scales were explored to ensure convergence.

[14] The primary impact of the X-ray photons is to set the spin temperature of the IGM gas. For scenarios with extremely high values of the X-ray luminosity, they can cause $\sim$10–15 per cent impact on the ionizations of the H I (Mesinger et al. 2013). In these extreme cases, the X-ray can provide some constraints from UV LFs via the baryon modifier $f_{\rm mod}$. We have visually checked the constraints and have found them to be negligible for our fiducial model.

[15] A single model evaluation takes $\sim$16 h on two 48-core nodes.

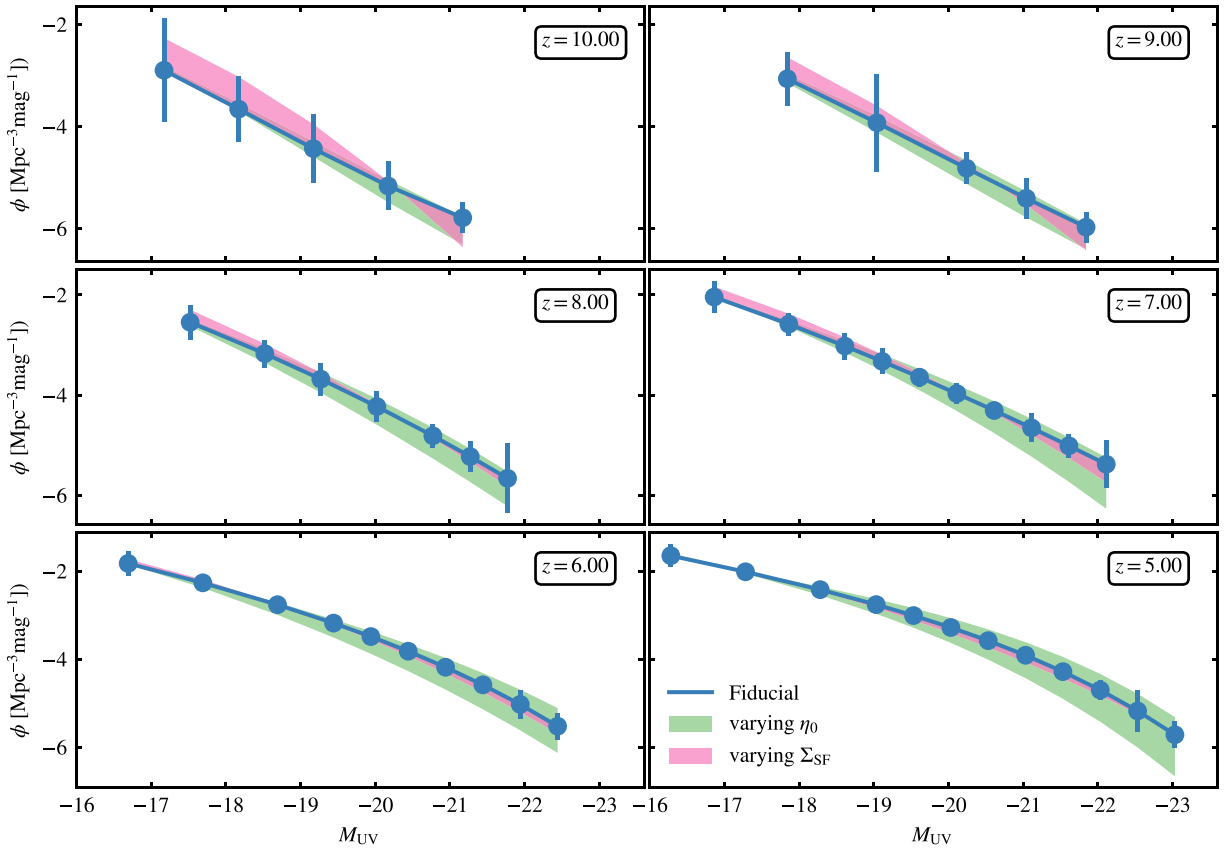

Figure 2. The solid blue curve shows the fiducial UV LFs from our calibrated simulation. The uncertainties on our UV LFs are equivalent to the fractional uncertainties from Bouwens et al. 2021. The shaded regions show the variation in the UV LFs as we vary the critical mass normalization ($\Sigma_{\rm SF}$; pink) and the efficiency of gas reheating due to SNe feedback (η_0; green), respectively. These parameters are varied by an order of magnitude about their fiducial values to explore their impact on the UV LFs and clearly demonstrate that including UV LFs in our Fisher matrix will improve our forecasted constraints as the range exceeds the 1σ observational uncertainty.

5 RESULTS

In this section, we report the quantitative constraints available with a mock observation using just the 21-cm PS and also combining the 21-cm PS with the UV LFs.

5.1 Forecasts from the 21-cm PS alone

In Fig. 3, we show the forecasts on our astrophysical parameter set from the 21-cm PS corresponding to a ∼1000 h observation with SKA1-low. The dark (light) contours correspond to the 1(2)σ 2D marginalized confidence intervals for each astrophysical parameter and the diagonal subplots show the 1D normalized marginal probability distribution function. The fifth column of table 1 lists the 1σ uncertainty on our parameters. The fractional uncertainties, $|\sigma(\theta_i)/\theta_i^{fid}|$, are given within brackets and are shown as blue squares in Fig. 5.

We obtain tight constraints ($\lesssim$10 per cent) for the X-ray parameters (luminosity $L_{\rm X}$/SFR and minimum X-ray photon energy escaping galaxies E_0), escape fraction normalization ($f_{\rm esc,0}$), and star formation efficiency ($\alpha_{\rm SF}$), while the SNe ejection efficiency (ϵ_0) is constrained to ∼25 per cent. On the other hand, the critical mass normalization ($\Sigma_{\rm SF}$) and the efficiency of SNe reheating (η_0) remain relatively unconstrained with ∼234 and ∼117 per cent fractional 1σ uncertainties, respectively. The relatively poor constraints on $\Sigma_{\rm SF}$ and η_0 are primarily because these parameters have negligible impact on the 21-cm PS.

As previously mentioned, our parameter set forms four groups of two with each group controlling a different aspect of galaxy properties.

(i) *X-ray parameters*: The 21-cm signal is very sensitive to the amount and energy of the X-ray photons in the early Universe. The 21-cm PS, therefore, provides tight constraints on the X-ray parameters, E_0 (∼11 per cent) and $L_{\rm X}$/SFR (∼10^{-2} per cent), in our model. These forecasts are consistent with similar works in the literature (e.g. Greig & Mesinger 2017; Park et al. 2019; Mason et al. 2023), which is unsurprising given they have the same X-ray implementation despite the differences in the source modelling (i.e. SAM).

(ii) *UV escape fraction*: $f_{\rm esc}$ is more sensitive to the normalization $f_{\rm esc,0}$ as opposed to the redshift power-law exponent ($\alpha_{\rm esc}$). This is also reflected in the derivative of the 21-cm PS with respect to these parameters (green and pink curves in Fig. A1). We thus forecast tighter constraints on $f_{\rm esc,0}$ (6.55 per cent) compared to $\alpha_{\rm esc}$ (66.93 per cent).

(iii) *Star formation*: Among the star formation parameters, the efficiency of star formation ($\alpha_{\rm SF}$) is highly constrained relative to the critical mass normalization ($\Sigma_{\rm SF}$). The primary impact of $\Sigma_{\rm SF}$ is to establish a critical mass threshold needed for the stars to start

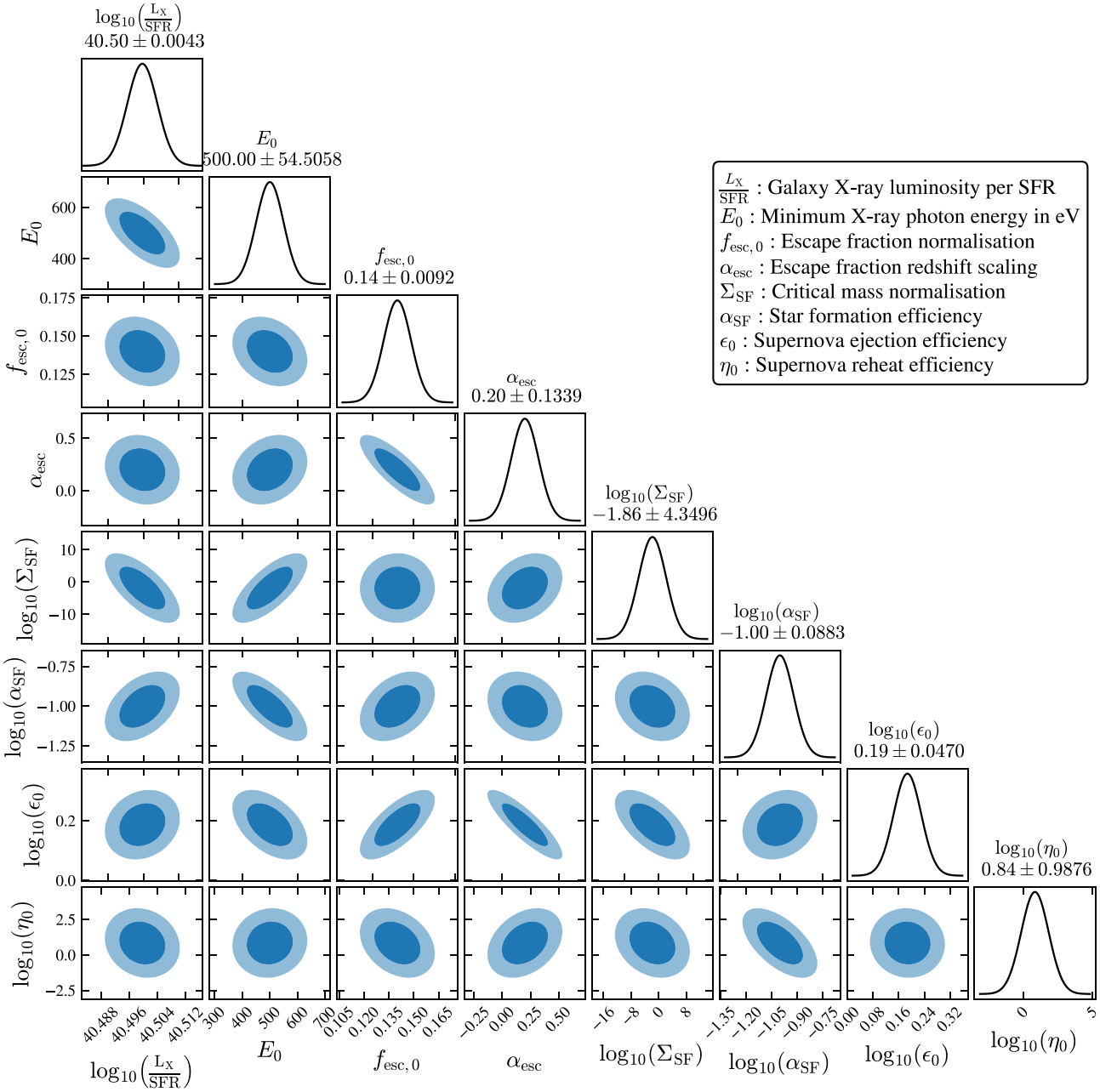

Figure 3. Constraints on our astrophysical model parameters from our Fisher matrix using a 1000 h mock observation with the SKA1-low. Dark (light) contours represent the 2D marginalized confidence intervals and the diagonal subplots show the 1D marginalized probability distribution functions of our parameters.

forming. This parameter thus has only a secondary role in the stellar mass content of galaxies as once a galaxy has accreted enough mass, the amount of stellar material is controlled by α_{SF} (see Section 2.2.1). Equation (2) also shows that these two parameters enter our model as a multiplicative term of the form $(1 - \Sigma_{SF})\alpha_{SF}$ adding to their degeneracy.

(iv) *SNe feedback*: Compared to the star formation parameters, we find that the SNe parameters are less constrained, with ∼25 per cent for the SNe ejection efficiency ϵ_0, while the efficiency of reheating by the SNe η_0 is only constrained to ∼117 per cent. Similar to Σ_{SF}, the low constraints on these parameters are due to the fiducial model values being such that the 21-cm signal is relatively insensitive to these processes.

5.2 Joint forecasts using the 21-cm PS and the UV LFs

We next add in the Fisher matrix corresponding to the UV LFs from six redshifts ∈ [5, 10]. As the UV LFs functions are sensitive to parameters that do not have a pronounced impact on the ionization morphology, the addition of the UV LFs into the analysis helps improve the overall constraints on the astrophysical model (Park et al. 2019). We show the impact of varying the two least constrained parameters when using just the 21-cm PS, Σ_{SF}, and η_0, on the UV LFs in Fig. 2. The green and pink shaded regions are from varying η_0 and Σ_{SF}, respectively, by an order of magnitude about their fiducial values (we point out that these two parameters are positive by definition). The variation in the UV LFs is larger than

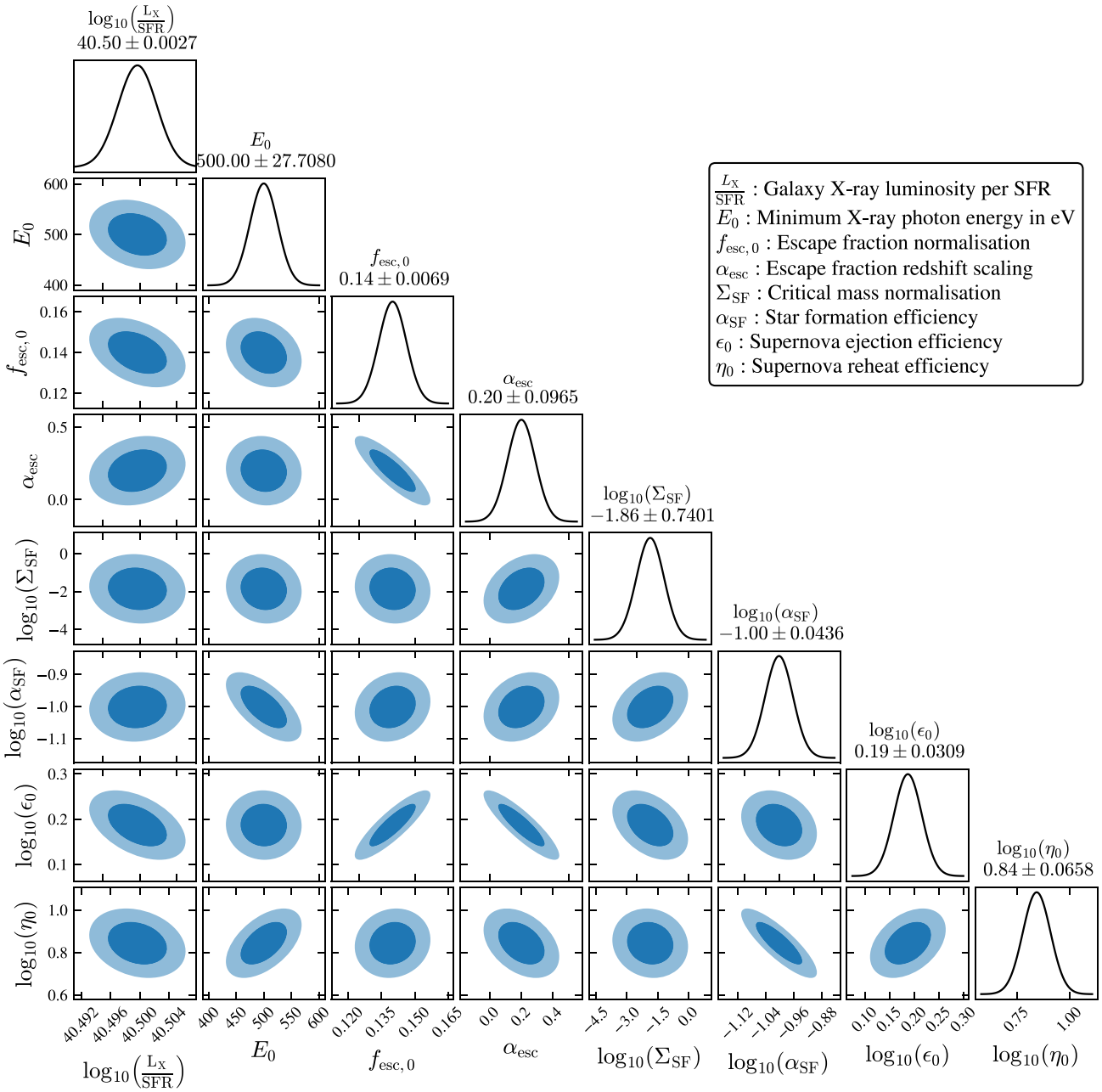

Figure 4. Same as Fig. 3, except that we have also added in constraints from the UV LFs. This removes some of the degeneracies between our parameters and results in tighter constraints.

the 1σ errors emphasising that including the UV LFs in our Fisher analysis will provide additional constraining power. As previously mentioned, we do not vary the X-ray parameters, L_X/SFR and E_0, while computing the UV LF Fisher matrix.

Fig. 4 shows the constraints from the joint analysis of the 21-cm PS and UV LFs, and the last column of Table 1 lists the forecasted 1σ uncertainty along with the fractional uncertainties for our model parameters. The green stars in Fig. 5 are the fractional uncertainties for the joint analysis of both the 21-cm PS and the UV LFs, and the orange crosses represent the same from just the UV LFs.[16] Figs 3 and 5 demonstrate that combining the UV LFs into the analyses helps to improve the constraints. This is most notable for parameters having a direct impact on the stellar mass of the galaxies i.e. the ones related to star formation and supernova feedback as UV LFs are more sensitive to these parameters compared to the 21-cm PS. This results in significant improvements in Σ_{SF} (from ∼234 to ∼40 per cent) and η_0 (from ∼117 to ∼8 per cent) for the joint case of both the 21-cm PS and the UV LFs as the degeneracies between stellar properties and escape fraction can be weakened. This then translates into improvements in other parameters.

The relatively larger improvement in Σ_{SF} compared to α_{SF} following the inclusion of information from the UV LFs stems from the breaking of parameter degeneracies. In Fig. 3 (21-cm PS only),

[16]In Fig. B2 we show the constraints from the UV LFs alone.

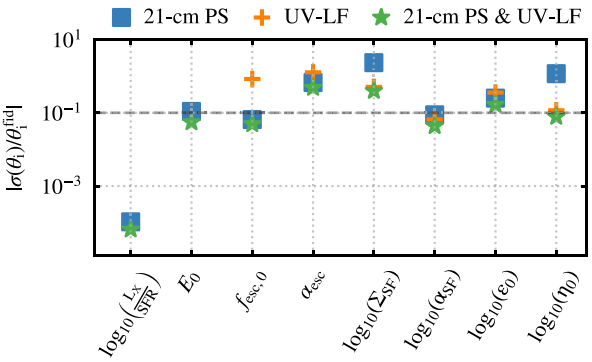

Figure 5. Fractional uncertainties on our eight free parameters. The vertical axis is the 1σ uncertainties divided by their fiducial values. The blue squares are from just the 21-cm PS, the orange crosses from just the UV LFs, and the green stars are from the joint analysis. While constructing the UV LFs Fisher matrix we do not consider the parameters controlling the X-ray luminosity of the galaxies, L_X/SFR, and E_0. The grey dotted line shows the 10 per cent fractional uncertainty limit.

$\Sigma_{\rm SF}$ is poorly constrained (highlighted by the large uncertainties), and $\Sigma_{\rm SF}$ and $\alpha_{\rm SF}$ are anticorrelated. In Fig. B2 (UV LFs only), $\Sigma_{\rm SF}$ is now more tightly constrained and positively correlated with $\alpha_{\rm SF}$, indicating the majority of $\Sigma_{\rm SF}$'s constraining power comes from the UV LF. Thus, the inclusion of UV LFs provide considerable improvements to the constraining power of $\Sigma_{\rm SF}$. For $\alpha_{\rm SF}$ on the other hand, it is almost equally well constrained both by the 21-cm PS (Fig. 3) and the UV LFs (Fig. B2). Thus combining the two observables provides modest improvements (dominated by the change in correlation).

5.3 Discussion of parameter degeneracies

Even though Fisher matrices implicitly make simplifying assumptions, such as Gaussian likelihoods and Gaussian errors, they nevertheless give useful insights. In this section, we explore the correlations and degeneracies among the model parameters. For brevity, we focus only on the results from the joint analysis of the UV LFs and the 21-cm PS (Fig. 4), noting that the trends are similar for the 21-cm PS alone (Fig. 3).

(i) *X-ray parameters*: L_X/SFR anticorrelates with the UV escape fraction normalization ($f_{\rm esc,0}$) and the SNe ejection efficiency (ϵ_0). E_0 shows an anticorrelation with the star formation efficiency ($\alpha_{\rm SF}$) and positively correlates with the SNe reheat efficiency (η_0).
These correlations can be understood from the impact of the X-rays on the EoR. X-rays can contribute, albeit a small fraction relative to the UV photons, to the ionization of the local IGM of a galaxy leading to photoionization regulation of the amount of neutral gas available for accretion on to the galaxy and hence subsequent star formation. Thus increasing L_X/SFR can be compensated by a decrease in the SNe feedback and/or the ionizing UV escape fraction. E_0 sets the lowest energy for escaping X-rays from the galaxies. An increase in E_0, therefore, implies less IGM ionization by the X-rays.

(ii) *UV escape fraction*: The correlation among $\alpha_{\rm esc}$ and $f_{\rm esc,0}$ is expected given the definition of the UV escape fraction ($f_{\rm esc}$; see equation (10)). The UV escape fraction, $f_{\rm esc}$, directly influences the local IGM ionization state, and hence the amount of baryonic infall into the galaxy for star formation. The amount of cold gas available for star formation is influenced by the SNe ejection efficiency which sets the amount of gas removed from the galaxy. An increase in $f_{\rm esc}$ therefore should be accompanied by a decrease in the SNe feedback. In light of this, the relatively strong positive correlation of $f_{\rm esc,0}$ with the supernova ejection efficiency ϵ_0 is interesting. This can be understood from the behaviour of the UV escape fraction (i.e. the combination of $f_{\rm esc,0}$ and $\alpha_{\rm esc}$) and the other physical processes. The positive correlation amongst the SNe parameters (η_0 & ϵ_0), as can be seen from equations (3–7) and Fig. B2, also plays a contributing factor. $\alpha_{\rm esc}$ is also anticorrelated with both η_0 and ϵ_0. It is therefore a combination of the very weak correlation of $f_{\rm esc,0}$ with η_0 and the anticorrelation with $\alpha_{\rm esc}$ that results in its positive correlation with ϵ_0. The comparatively tighter correlation of the escape fraction parameters with the SNe parameters compared to the X-ray parameters reflects the relative importance of the UV photons over the X-ray photons in the IGM ionization state.

(iii) *Star formation*: As noted, we report correlations between the star formation efficiency $\alpha_{\rm SF}$ and the minimum X-ray photon energy E_0.
The strong correlation between $\alpha_{\rm SF}$ and SNe reheat efficiency η_0 is expected as they are two of the parameters impacting the stellar mass in a galaxy.
On the other hand, the correlation between $\alpha_{\rm SF}$ and the critical mass normalization $\Sigma_{\rm SF}$ is surprisingly weak given equation (2). This is because of the relatively small value of $\Sigma_{\rm SF}$. $\Sigma_{\rm SF}$ fixes the critical mass of the cold gas needed for star formation to commence in a galaxy. The small value of the parameter is justified on the physical grounds that a larger value will result in lower available gas for star formation.

(iv) SNe *feedback*: For completeness, we again point out the correlations between the SNe ejection (ϵ_0) and reheat (η_0) efficiencies, the strong correlations of ϵ_0 with $f_{\rm esc,0}$ and E_0, and that of η_0 with $\alpha_{\rm SF}$.

6 CONCLUSION

Using the semi-analytic galaxy formation model MERAXES we perform a Fisher matrix analysis to forecast the constraints on physical properties of galaxy formation and reionization that will be available from future 21-cm PS observations. Specifically, we use the 210 h^{-1} Mpc cosmological simulation resolving all atomically cooled haloes (L210_AUG of Balu et al. 2023) down from $z = 20$.

SAMs are unique in enabling computationally efficient exploration of the underlying parameter space corresponding to the complex astrophysics of galaxy formation and evolution. We focused on eight free parameters in our model that directly impact the X-ray luminosity, UV escape fraction, star formation rate, and SNe feedback of the galaxies. We constructed a mock observation of the 21-cm PS, focusing on a 1000 h observation with the forthcoming SKA1-low. The observational uncertainty was modelled assuming foreground wedge avoidance using the PYTHON package 21CMSENSE. Using the Fisher matrix formalism, we find that four (five) out of the eight parameters can be constrained to within $\lesssim$10 ($\lesssim$50) per cent using the 21-cm PS alone from the EoR. Specifically, we forecast constraints on our X-ray parameters (the luminosity L_X/SFR and the minimum energy of the photon escaping the early galaxies E_0) that are comparable to similar works in the literature. We also forecast tight constraints on parameters controlling the star formation efficiency ($\alpha_{\rm SF}$) as well as the normalization of the UV escape fraction ($f_{\rm esc,0}$) of the early galaxies. On the other hand, SNe feedback parameters remain largely unconstrained reflecting that the 21-cm PS is relatively insensitive to them. The complex astrophysics of the early galaxy formation and evolution is captured in the degeneracies

and correlations among the model parameters. Of particular interest are the correlations among the UV escape fraction and SNe feedback, and those between the star formation efficiency and X-ray parameters of the galaxies.

To improve the overall constraining power of our analysis we added the Fisher matrix corresponding to the UV LFs from redshifts $z \in [5, 10]$. This results in an improvement in all of our parameter forecasts, most notably the critical mass normalization $\Sigma_{\rm SF}$ and the SNe reheat efficiency η_0. This is not surprising as these parameters primarily control the stellar mass content of the galaxies to which the UV LFs are very sensitive. Incorporating the UV LFs into the analyses results in five of our parameters being constrained to $\lesssim$10 per cent and all eight of them being to within $\lesssim$50 per cent. Our forecasts illustrate that detailed observations of reionization with the SKA will be valuable in constraining the astrophysics of the early galaxies.

ACKNOWLEDGEMENTS

We thank the referee for their detailed comments which improved the quality of this manuscript. SB thanks Yuxiang Qin for the helpful discussions which assisted this work. This research was supported by the Australian Research Council Centre of Excellence for All Sky Astrophysics in 3 Dimensions (ASTRO 3D), through project #CE170100013. Part of this work was performed on the OzSTAR national facility at the Swinburne University of Technology. The OzSTAR program partially receives funding from the Astronomy National Collaborative Research Infrastructure Strategy (NCRIS) allocation provided by the Australian Government. This research also made use of resources from the National Computational Infrastructure (NCI Australia), another NCRIS-enabled capability supported by the Australian Government.

Software citations: This research relies heavily on the PYTHON (Van Rossum & Drake 1995) open source community, in particular, NUMPY (Harris et al. 2020), MATPLOTLIB (Hunter 2007), SCIPY (Virtanen et al. 2020), H5PY, JUPYTER (Granger & Pérez 2021), and PANDAS (pandas development team 2023).

DATA AVAILABILITY

The data underlying this article will be shared on reasonable request to the corresponding author.

REFERENCES

Ahn K., Iliev I. T., Shapiro P. R., Srisawat C., 2015, MNRAS, 450, 1486
Albrecht A. et al., 2009, preprint (arXiv.0901.0721)
Balu S., Greig B., Qiu Y., Power C., Qin Y., Mutch S., Wyithe J. S. B., 2023, MNRAS, 520, 3368
Barkana R., Loeb A., 2001, Phys. Rep., 349, 125
Battaglia N., Trac H., Cen R., Loeb A., 2013, ApJ, 776, 81
Becker G. D., Aloisio A. D.., Christenson H. M., Zhu Y., Worseck G., Bolton J. S., 2021, MNRAS, 508, 1853
Bevins H. T. J., Heimersheim S., Abril-Cabezas I., Fialkov A., Acedo E. d. L., Handley W., Singh S., Barkana R., 2023, preprint (arXiv.2301.03298)
Bond J. R., Cole S., Efstathiou G., Kaiser N., 1991, ApJ, 379, 440
Bouwens R. J. et al., 2015, ApJ, 803, 34
Bouwens R. J. et al., 2021, AJ, 162, 47
Bower R. G., 1991, MNRAS, 248, 332
Charlot S., Fall S. M., 2000, ApJ, 539, 718
Choudhury T. R., Paranjape A., 2018, MNRAS, 481, 3821
Das A., Mesinger A., Pallottini A., Ferrara A., Wise J. H., 2017, MNRAS, 469, 1166
Datta A., Bowman J. D., Carilli C. L., 2010, ApJ, 724, 526
Deboer D. R. et al., 2017, Publ. Astron. Soc. Pac., 129, 045001
Elahi P. J., Cañas R., Poulton R. J., Tobar R. J., Willis J. S., Lagos C. D. P., Power C., Robotham A. S., 2019a, Publ. Astron. Soc. Aust., 36, 12
Elahi P. J., Poulton R. J., Tobar R. J., Cañas R., Lagos C. D. P., Power C., Robotham A. S., 2019b, Publ. Astron. Soc. Aust., 36, 18
Field G. B., 1958, PIRE, 46, 240
Furlanetto S. R., Zaldarriaga M., Hernquist L., 2004, ApJ, 613, 1
Furlanetto S. R., Peng Oh S., Briggs F. H., 2006, Phys. Rep., 433, 181
Geil P. M. et al., 2016, MNRAS, 462, 804
Ghara R., Choudhury T. R., Datta K. K., 2015, MNRAS, 447, 1806
Gnedin N. Y., Madau P., 2022, Living Rev. Sol. Phys., 8, 3
Granger B. E., Pérez F., 2021, Comput. Sci. Eng., 23, 7
Greig B., Mesinger A., 2015, MNRAS, 449, 4246
Greig B., Mesinger A., 2017, MNRAS, 472, 2651
Greig B., Mesinger A., 2018, MNRAS, 477, 3217
Guo Q. et al., 2011, MNRAS, 413, 101
Harris C. R. et al., 2020, Nature, 585, 357
Hassan S., Davé R., Finlator K., Santos M. G., 2016, MNRAS, 457, 1550
Hunter J. D., 2007, Comput. Sci. Eng., 9, 90
Hutter A., Dayal P., Yepes G., Gottlöber S., Legrand L., Ucci G., 2021, MNRAS, 503, 3698
Iliev I. T., Mellema G., Ahn K., Shapiro P. R., Mao Y., Pen U. L., 2014, MNRAS, 439, 725
Kauffmann G., 1996, MNRAS, 281, 475
Kaur H. D., Gillet N., Mesinger A., 2020, MNRAS, 495, 2354
Kimm T., Katz H., Haehnelt M., Rosdahl J., Devriendt J., Slyz A., 2017, MNRAS, 466, 4826
Koopmans L. V. et al., 2014, Proc. Sci., Advancing Astrophysics with the Square Kilometre Array (AASKA14) - Session 1: Epoch of Reionisation. Sissa, Trieste, Pos #1
Kroupa P., 2002, Science, 295, 82
Lacey C., Cole S., 1993, MNRAS, 262, 627
Leitherer C. et al., 1999, ApJS, 123, 3
Leitherer C., Ortiz Otálvaro P. A., Bresolin F., Kudritzki R.-P., Lo Faro B., Pauldrach A. W. A., Pettini M., Rix S. A., 2010, ApJS, 189, 309
Leitherer C., Ekström S., Meynet G., Schaerer D., Agienko K. B., Levesque E. M., 2014, ApJS, 212, 14
Ma Q.-B., Ghara R., Ciardi B., Iliev I. T., Koopmans L. V. E., Mellema G., Mondal R., Zaroubi S., 2023, MNRAS, 522, 3284
Maity B., Choudhury T. R., 2022, MNRAS, 515, 617
Mason C. A., Muñoz J. B., Greig B., Mesinger A., Park J., 2023, MNRAS, 524, 4711
McQuinn M., 2012, MNRAS, 426, 1349
McQuinn M., Zahn O., Zaldarriaga M., Hernquist L., Furlanetto S. R., 2006, ApJ, 653, 815
Mertens F. G. et al., 2020, MNRAS, 493, 1662
Mesinger A., 2019, The Cosmic 21-cm Revolution: Charting the first billion years of our Universe. IOP Publishing
Mesinger A., Furlanetto S., Cen R., 2011, MNRAS, 411, 955
Mesinger A., Ferrara A., Spiegel D. S., 2013, MNRAS, 431, 621
Morales M. F., 2005, ApJ, 619, 678
Morales M. F., Wyithe J. S. B., 2010, ARA&A, 48, 127
Murray S., Greig B., Mesinger A., Muñoz J., Qin Y., Park J., Watkinson C., 2020, J. Open Source Softw., 5, 2582
Mutch S. J., Geil P. M., Poole G. B., Angel P. W., Duffy A. R., Mesinger A., Wyithe J. S. B., 2016, MNRAS, 462, 250
Mutch S. J., Greig B., Qin Y., Poole G. B., Wyithe J. S. B., 2023, preprint (arXiv.2303.07378)
Park J., Mesinger A., Greig B., Gillet N., 2019, MNRAS, 484, 933
Parsons A., Pober J., McQuinn M., Jacobs D., Aguirre J., 2012, ApJ, 753, 81
Parsons A. R. et al., 2014, ApJ, 788, 106
Planck Collaboration, 2016, A&A, 594, A13
Planck Collaboration, 2020, A&A, 641, A6
Pober J. C. et al., 2013, AJ, 145, 65
Pober J. C. et al., 2014, ApJ, 782, 66
Prelogović D., Mesinger A., 2023, MNRAS, 524, 4239
Pritchard J. R., Loeb A., 2012, Rep. Prog. Phys., 75, 086901

Qin Y. et al., 2017, MNRAS, 472, 2009
Qin Y., Mesinger A., Park J., Greig B., Muñoz J. B., 2020, MNRAS, 495, 123
Qin Y., Mesinger A., Greig B., Park J., 2021a, MNRAS, 501, 4748
Qin Y., Mesinger A., Bosman S. E., Viel M., 2021b, MNRAS, 506, 2390
Qiu Y., Mutch S. J., da Cunha E., Poole G. B., Stuart Wyithe J. B., 2019, MNRAS, 489, 1357
Qiu Y., Mutch S. J., Elahi P. J., Poulton R. J. J., Power C., Wyithe J. S. B., 2020, MNRAS, 500, 493
Schaller M., Gonnet P., Draper P. W., Chalk A. B. G., Bower R. G., Willis J., Hausammann L., 2018, Astrophysics Source Code Library, record ascl:1805.020
Seiler J., Hutter A., Sinha M., Croton D., 2019, MNRAS, 487, 5739
Sobacchi E., Mesinger A., 2013, MNRAS, 432, 3340
Sobacchi E., Mesinger A., 2014, MNRAS, 440, 1662
Somerville R. S., Davé R., 2015, Annu. Rev. Astron. Astrophys., 53, 51
Song M. et al., 2016, ApJ, 825, 5
Songaila A., Cowie L. L., 2010, ApJ, 721, 1448
Stefanon M., Bouwens R. J., Labbé I., Illingworth G. D., Gonzalez V., Oesch P. A., 2021, ApJ, 922, 29
Tegmark M., Taylor A. N., Heavens A. F., 1997, ApJ, 480, 22
The HERA Collaboration, 2022, preprint (arXiv.2210.04912)
The pandas development team, 2023, pandas-dev/pandas: Pandas, available at: https://zenodo.org/record/7857418
Thompson A. R., Moran J. M., Swenson G. W., Jr, 2017, Interferometry and Synthesis in Radio Astronomy, 3rd edn. Springer, Berlin
Tingay S. J. et al., 2013, Publ. Astron. Soc. Aust., 30, e007
Tinker J. L., Robertson B. E., Kravtsov A. V., Klypin A., Warren M. S., Yepes G., Gottlöber S., 2010, ApJ, 724, 878
Trott C. M. et al., 2020, MNRAS, 493, 4711
Van Haarlem M. P. et al., 2013, A&A, 556, A2
Van Rossum G., Drake F. L., Jr, 1995, Python reference manual. Centrum voor Wiskunde en Informatica Amsterdam
Virtanen P. et al., 2020, Nat. Meth., 17, 261
Visbal E., Bryan G. L., Haiman Z., 2020, ApJ, 897, 95
Wouthuysen S. A., 1952, AJ, 57, 31
Wyithe J. S. B., Loeb A., 2004, Nature, 432, 194
Yeh J. Y.-C. et al., 2023, MNRAS, 520, 2757

APPENDIX A: DERIVATIVES OF THE 21-CM PS

In this section, we show the derivatives of our primary statistics i.e. the 21-cm PS (Fig. A1). These derivatives are computed by perturbing the L210_AUG simulation about the fiducial model, one parameter θ_i at a time. These are then used to compute the Fisher matrix (see equation 23). Parameters corresponding to similarly shaped derivatives will be degenerate. Fig. A1 shows these derivatives $[\partial\Delta^2_{21}/\partial\theta_i]$ weighted by the noise powers $[\varepsilon(k, z)]$, i.e. $\frac{1}{\varepsilon}\frac{\partial\Delta^2_{21}}{\partial\theta_i}$. We have employed a 'symmetric log' scaling on the vertical axis in the figure with the scale being linear $\in [-10, 10]$ and log-scale otherwise.

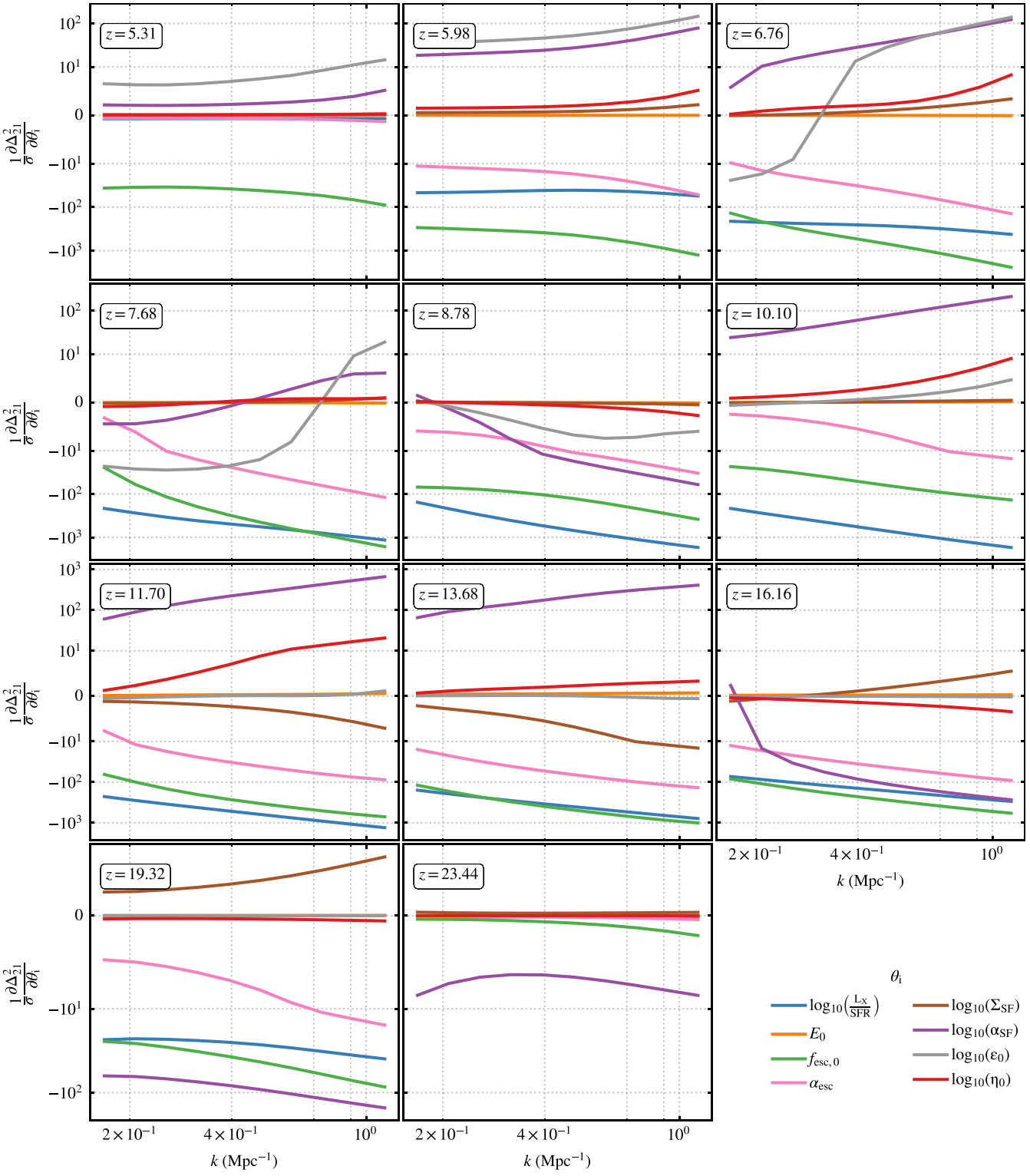

Figure A1. The derivatives of the 21-cm PS $[\partial\Delta^2_{21}/\partial\theta_i]$ with respect to the parameters varied in this work. The derivatives are weighted by the noise levels $[\sigma(k, z)]$. The vertical axes is linear $\in [-10, 10]$ and log-scale otherwise.

APPENDIX B: ADDING IN THE UV LFS

This section shows the analysis using only the UV LFs. Fig. B1 shows the derivatives of the UV LFs, computed by perturbing the L210_AUG simulation about the fiducial model, one parameter θ_i at a time. These are then used to compute the Fisher matrix. We do not vary the X-ray parameters, L_X/SFR and E_0, for the UV LFs analysis as they do not have an impact on the UV LFs. Parameters corresponding to similarly shaped derivatives will be degenerate.

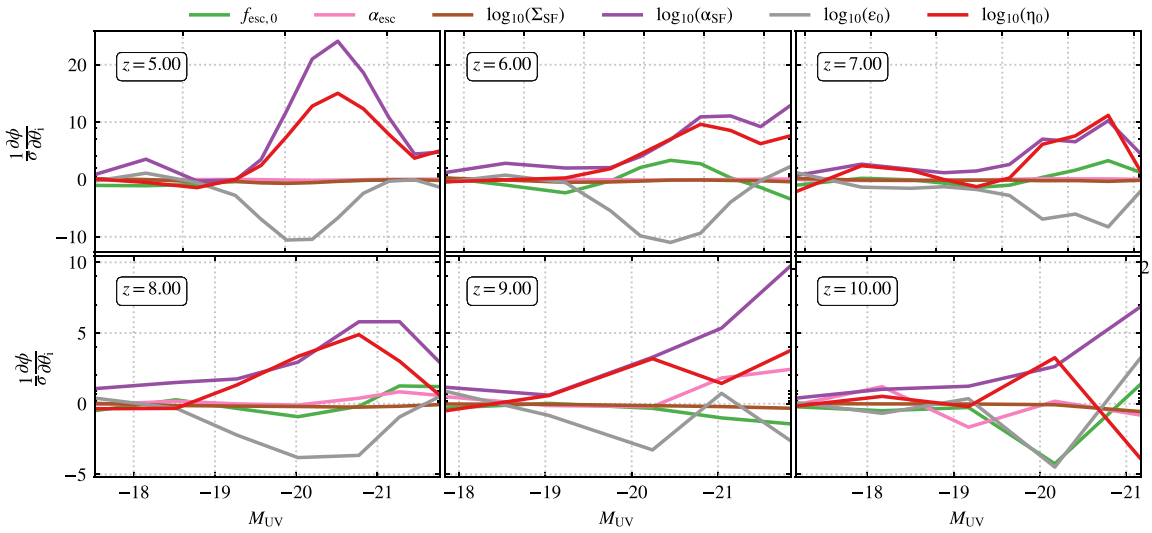

Figure B1. The derivatives of the UV LFs $[\partial\phi/\partial\theta_i]$ with respect to the parameters varied in this work. The derivatives are weighted by the noise levels $[\sigma(M_{UV}, z)]$.

Fig. B1 shows these derivatives $[\partial\phi/\partial\theta_i]$ weighted by the noise powers $[\sigma(M_{UV}, z)]$, i.e. $\frac{1}{\sigma}\frac{\partial\phi}{\partial\theta_i}$.

In Fig. B2 we show the forecasted constraints from the UV LFs Fisher matrix. The dark (light) contours correspond to the 1(2)σ 2D marginalized confidence intervals for each astrophysical parameter and the diagonal subplots show the 1D normalized marginal probability distribution function.

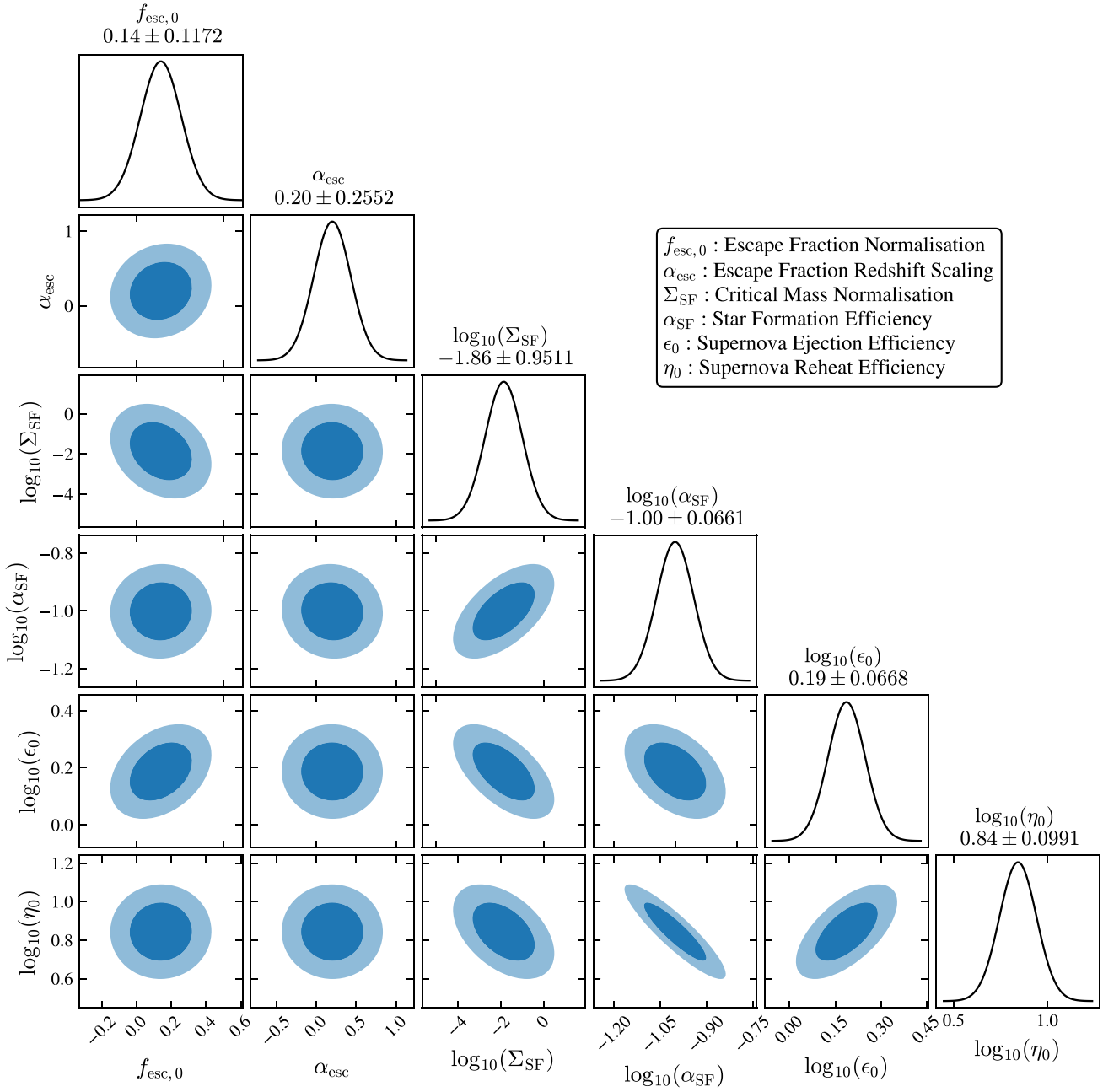

Figure B2. Constraints on our astrophysical model parameters from our Fisher matrix analysis using only the UV LFs. Dark (light) contours represent the 2D marginalized confidence intervals and the diagonal subplots show the 1D marginalized probability distribution functions of our parameters. Note that while computing the UV LFs Fisher matrices we do not vary the X-ray parameters (see text for more details).

This paper has been typeset from a TEX/LATEX file prepared by the author.